10-Fold Quantum Yield Improvement of Ag₂S Nanoparticles by Fine Compositional Tuning

Alicia Ortega-Rodríguez, Yingli Shen, Irene Zabala Gutierrez, Harrison D. A. Santos, Vivian Torres Vera, Erving Ximendes, Gonzalo Villaverde, José Lifante, Christoph Gerke, Nuria Fernández, Oscar G. Calderón, Sonia Melle, José Marques-Hueso, Diego Mendez-Gonzalez, Marco Laurenti, Callum M. S. Jones, Juan Manuel López-Romero, Rafael Contreras-Cáceres,* Daniel Jaque,* and Jorge Rubio-Retama*

Cite This: *ACS Appl. Mater. Interfaces* 2020, 12, 12500−12509

Read Online

ACCESS | Metrics & More | Article Recommendations | Supporting Information

ABSTRACT: Ag₂S semiconductor nanoparticles (NPs) are near-infrared luminescent probes with outstanding properties (good biocompatibility, optimum spectral operation range, and easy biofunctionalization) that make them ideal probes for in vivo imaging. Ag₂S NPs have, indeed, made possible amazing challenges including in vivo brain imaging and advanced diagnosis of the cardiovascular system. Despite the continuous redesign of synthesis routes, the emission quantum yield (QY) of Ag₂S NPs is typically below 0.2%. This leads to a low luminescent brightness that avoids their translation into the clinics. In this work, an innovative synthetic methodology that permits a 10-fold increment in the absolute QY from 0.2 up to 2.3% is presented. Such an increment in the QY is accompanied by an enlargement of photoluminescence lifetimes from 184 to 1200 ns. The optimized synthetic route presented here is based on a fine control over both the Ag core and the Ag/S ratio within the NPs. Such control reduces the density of structural defects and decreases the nonradiative pathways. In addition, we demonstrate that the superior performance of the Ag₂S NPs allows for high-contrast in vivo bioimaging.

KEYWORDS: Ag₂S/Ag nanoparticles, fluorescent probes, synthesis optimization, PL lifetime, PLQY, NIR-II imaging
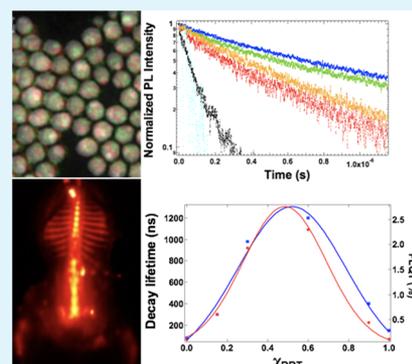
1. INTRODUCTION

Biomedical imaging techniques are used routinely in clinical practice as they provide physiological information of organs/tissues of living beings that is, otherwise, unreachable.[1,2] These noninvasive techniques allow the diagnosis and/or prognosis of different diseases and have gained increasing interest in clinical and medical research. Among them, computed tomography (CT), positron emission tomography (PET) or single-photon emission tomography (SPECT), magnetic resonance imaging (MRI), ultrasonography (Echo), and optical coherent tomography are by far the most used techniques. However, some drawbacks such as the use of ionizing radiation (CT, PET, and SPECT), limited spatial resolution (MRI, Echo, and PET), poor temporal resolution (CT, MRI, PET, and SPECT), and complex and expensive instrumentation restrict their access to third-level hospitals.[3,4]

Some of these drawbacks are overcome by near-infrared (NIR) fluorescent imaging in the so-called second NIR window, which ranged between 1000 and 1700 nm and characterized by the reduction of the scattering and absorption of tissues.[5,6] In vivo imaging in this spectral range has been widely demonstrated to provide better imaging resolution at larger depths into tissues.[7] The simplicity of the instrumenta-

tion as well as the high spatial and temporal resolution has facilitated, for instance, its use in medical research, where animal models are used to study the localization and evolution of diseases, thus facilitating a successful translation from research to clinical practice.[8,9] However, apart from being biocompatible, one of the major challenges to widen its application is related to the low quantum yield (QY) of most of the NIR fluorescent probes. For instance, Dai's group has reported organic compounds that emit in the NIR-II region, which can be used as fluorescent NIR-II probes.[10] Among them, CH1055, a conjugated organic molecule with good biological features, has shown a QY of 0.3%,[11] while other organic compounds, such as cholate-functionalized single-wall carbon nanotubes, have shown differences in QYs from exchanged- to cholate-SWNT samples of 0.84%.[12] Inorganic nanoparticles (NPs) based on heavy metal ions such as PbS or

CdHgTe have excellent fluorescent properties in the NIR-II region with a QY of about 40%;[13,14] however, these classes of NPs have been discarded because of their known acute and chronic toxicity.[15,16]

Silver chalcogenides can be considered as promising alternative candidates for NIR-II fluorescent imaging because of their negligible toxicity and high photostability.[17−19] However, their low luminescence brightness is still a big obstacle that limits their application for high-contrast, deep tissue in vivo imaging. Many works dealing with Ag_2S NP obtain QY as high as 10%;[20,21] however, most of these results are obtained by comparison with NIR-II fluorescent dyes that do not match with the absolute QYs measured with an integrating sphere and which are typically below 1%.[22] These low QYs agree with short photoluminescence (PL) lifetimes observed in these NP, ranging between 50 and 200 ns, which reveal the dominant role of nonradiative pathways within the emission process.[23,24] These nonradiative processes are associated with the presence of certain regions on the surface of the NP that act as charge acceptors, dissociating excitons and therefore reducing the PL efficiency.[25] Some of these traps are related to variations in solvent or surface-bound coordinating ligands (dangling bonds) that influence the steady-state, time-resolved PL and QY.[26] In addition, structural defects in the crystalline structure can also strongly affect the PL efficiency of the NPs because they induce the formation of midgap states that favor non-PL pathways and reduce the PL efficiency of the NPs.[27] Furthermore, in the case of Ag_2S NPs, the high redox potential of silver ions and the high temperature used during their synthesis can lead to the formation of a metallic silver core when the reaction is carried out in the presence of amines, forming Ag^+−amine complexes that are highly reactive and can form Ag_2S as well as Ag NPs.[28,29] To minimize the formation of the metallic silver core, different authors have proposed to remove, totally or partially, the presence of amine-bearing molecules and use dodecanethiol instead, thereby reducing the reactivity and passivating the surface of the NPs.[30] However, the resulting NPs still presented low QY[31] as well as short PL lifetimes.[32,33]

In this work, we have developed a new synthesis route toward the improvement of the fluorescence properties of Ag_2S NPs. A systematic study of the steady-state luminescence, emission lifetime, and absolute QYs of NPs with different metallic silver contents demonstrates that the presence of a specific amount of metallic silver within the NPs increases the QY of the NPs by more than 1 order of magnitude. This increment is concomitant with an enlargement of the PL lifetime which scales from 180 to 1220 ns as well as an emission red shift of the produced Ag_2S/Ag NPs. The potential use of the improved Ag_2S NPs for high-contrast in vivo imaging in the second biological window has also been evaluated.

2. EXPERIMENTAL SECTION

2.1. Chemicals. Silver nitrate (99%), sodium diethyldithiocarbamate (NaDDTC) (ACS reagent grade), oleylamine (70%) (OLA), 1-dodecanethiol (≤98%) (DDT), 11-mercaptoundecanoic acid (95%) (MUA), $CHCl_3$ (99.6%), ethanol (99.9%), N-(3-(dimethylamino)-propyl)-N′-ethylcarbodiimide hydrochloride (EDC) (99%), N-hydroxysulfosuccinimide sodium salt (sulfo-NHS) (98%), O-(2-aminoethyl)-O′-methyl-polyethylene glycol (PEG-NH_2, M_w = 5000 g/mol), and phosphate-buffered saline (PBS) tablets were purchased from Sigma-Aldrich and used as received. Commercial Ag_2S-PEG NPs were bought from NIR Optics Technology.

2.2. Characterization. Transmission electron microscopy (TEM) studies were carried out using a TEM Talos F200X operated at 80 kV. Zeta potential experiments were carried out using a Malvern Nano-ZS. The Fourier transform infrared (FTIR) spectra were obtained using a Nicolet IR200 FTIR spectrometer. X-ray diffraction (XRD) patterns were recorded on a Philips X'pert diffractometer (Cu Kα radiation, 45 kV, and 40 mA). Data were collected from $2\theta = 20−90°$ with a step size of 0.02° and a normalized count time of 1 s/step. The emission spectra upon illuminating the samples with an 800 nm CW laser were collected with an Andor iDus InGaAs 491 cooled to −90 °C. The absolute PL QY was measured with a calibrated spectrofluorometer (Edinburgh Instruments, FLS920) equipped with an integrating sphere (Jobin-Yvon). A Xe lamp has been used as the excitation source and filtered with a long-pass filter (610 nm) and a monochromator (wavelength: 800 nm, bandwidth: 20 nm). Luminescence was detected by a liquid-nitrogen-cooled NIR photomultiplier tube (Hamamatsu, R5509-72). The QY has been calculated by dividing the total number of emitted photons in the 900−1700 nm range by the total number of absorbed photons at 800 nm. Luminescence decay curves were obtained by exciting the colloidal suspensions of NPs by an OPO oscillator (Lotis) tuned to 800 nm, which provides 8 ns pulses at a repetition rate of 10 Hz. Fluorescence intensity was detected with a Peltier cooled photomultiplier tube with enhanced sensitivity in the NIR-II (Hamamatsu R5509-73). The contribution of scattered laser radiation was removed by using two band-pass filters (FEL850 from Thorlabs) and a high-brightness monochromator (Shamrock 320 from Andor). The time evolution of the fluorescence signal was finally recorded and averaged by a digital oscilloscope (LeCroy WaveRunner 6000).

High-angle annular dark-field (HAADF) scanning TEM (STEM) and energy-dispersive X-ray (EDX) mappings were conducted by using a FEI Talos F200X (FEI, USA) coupled to an EDX detector. The samples for TEM were prepared by adding 10 μL of each dispersion on a Cu grid with a carbon support membrane, followed by drying.

2.3. In Vivo Imaging. NIR-II in vivo images were obtained in a homemade NIR-II system. A fiber-coupled diode laser operating at 800 nm was used as the excitation source (LIMO30-F200-DL808). The illumination intensity was controlled via adjustment of diode current. An anesthetized mouse was placed on a homemade temperature-controlled plate operating at 36 °C. The NIR-II fluorescence image was acquired with a Peltier cooled InGaAs camera (Xeva 320 from Xenics). The InGaAs detector was cooled down to −40 °C. Two long-pass filters (FEL850 from Thorlabs) were used to remove the background signal generated by the scattered laser radiation.

In vivo experiments were approved by the regional authority for animal experimentation of Comunidad de Madrid and were conducted in agreement with the Universidad Autónoma de Madrid (UAM) Ethics Committee, in compliance with the European Union directives 63/2010UE and Spanish regulation RD 53/2013. For this study, a total of 15 CD1 female mice (8−14 weeks old, weighing 25−39 g) bred at the animal facility at UAM were used. The mice were anesthetized prior to the imaging experiments in an induction chamber with a continuous flow of 4% isoflurane (Forane, AbbVie Spain, S.L.U) in 100% oxygen until loss of righting reflex was confirmed and breathing rhythm was significantly slowed. Anesthesia was maintained throughout the experiments by means of facemask inhalation of 1.5% isoflurane and the core body temperature was maintained at 36 ± 1 °C, as measured with a rectal probe, using a heating pad.

2.4. Synthesis of Ag_2S/Ag-PEG NPs. The synthesis of the Ag_2S/Ag-PEG NPs was carried out in different steps as explained in the following sections.

2.4.1. Synthesis of Ag_2S/Ag NPs. The production of Ag_2S/Ag NPs was carried out as follows: a given amount of Ag(DDTC) (typically 25 mg, 0.1 mmol) was added into a two-neck round-bottom flask at room temperature, which contained 5 mL of a solvent mixture based on OLA and DDT. Table S1 shows the solvent mole fraction (χ_{DDT}) used in each synthesis, where $\chi_{DDT} = [n_{DDT}/(n_{DDT} + n_{OLA})]$. Once all
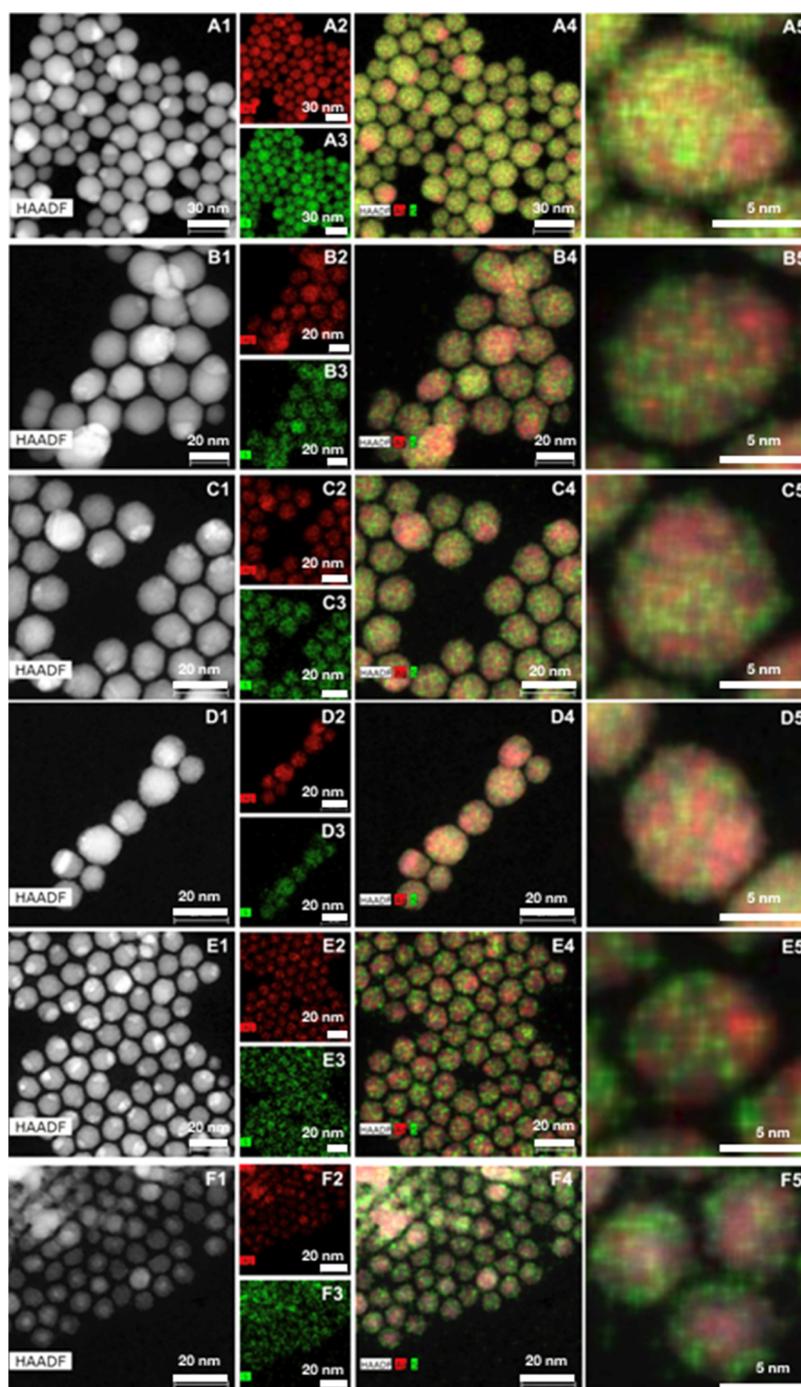
Figure 1. HAADF−STEM micrographs of NPs obtained under different synthetic conditions (from A1 to F1). The insets from A2 to F2 represent the EDS elemental mapping of silver, while the insets from A3 to F3 depict the EDS elemental mapping of sulfur. From A4 to F4, merged figures resulting from the HAADF−STEM and EDS elemental analysis are showed. The insets from A5 to F5 show detailed magnifications of the merged EDS and HAADF−STEM micrographs.

the reagents were introduced into the flask, the mixture was subjected to vacuum for 10 min to remove air and then filled with N_2. After that, the mixture was heated to 190 °C under slow magnetic stirring with a heating rate of 20 °C/min. The reaction was kept for 1 h and subsequently cooled down naturally. The synthesized NPs were collected by addition of ethanol, which reduces the colloidal stability of the NPs. To do that, 10 mL of ethanol was added to the raw product and centrifuged at 10,000 rpm for 10 min; this process was repeated twice. Finally, the as-prepared product was dispersed in 10 mL of chloroform and stored for further steps.

2.4.2. PEGylation of Ag_2S/Ag Heterodimers. With the aim of providing hydrophilicity to the synthesized NPs, they were treated with MUA. This molecule can displace the hydrophobic ligands attached on the surface of the NPs and introduce carboxylic groups on the surface of the NPs, thereby providing good colloidal stability in water. With that purpose, 20 mg (0.1 mmol) of MUA was added to a 1 mL dispersion containing 1 mg/mL of Ag_2S/Ag NPs in chloroform at room temperature. After that, the mixture was sonicated in an ultrasonic bath for 10 min until the Ag_2S/Ag NPs lose their colloidal stability and precipitated at the bottom of the flask. Then, the precipitate was collected and dispersed in 1 mL of PBS at pH 7.4.
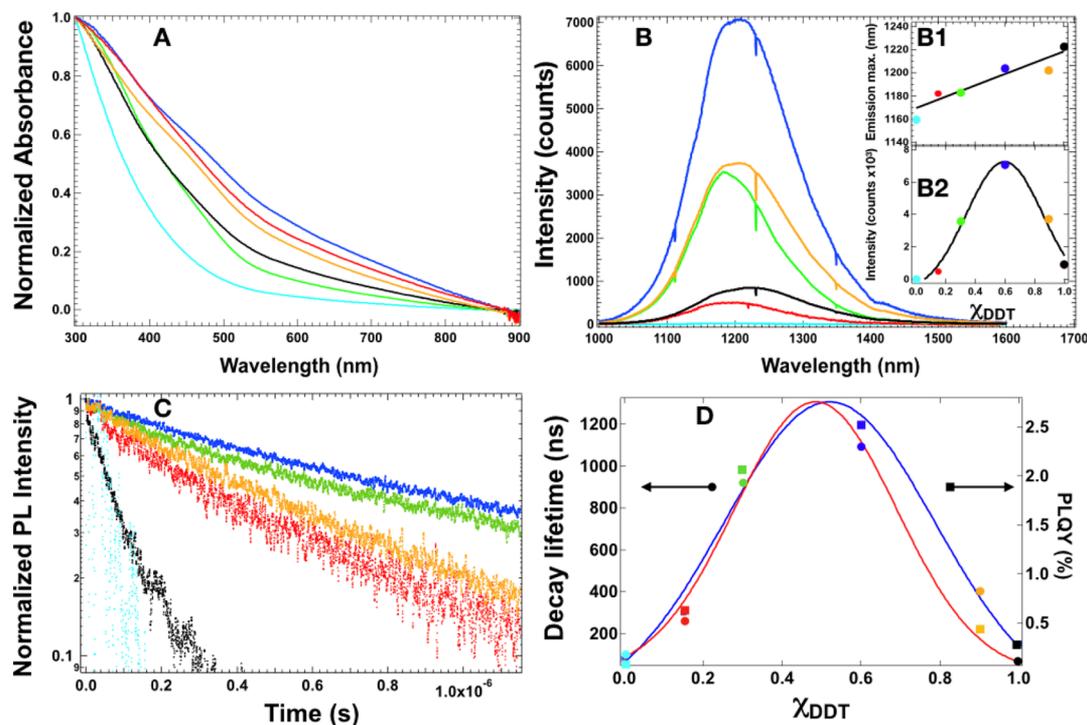
Figure 2. (A) Normalized UV−vis spectra of the NPs synthesized under different solvent ratios. (B) PL spectra of the NPs synthesized under different conditions dispersed in CHCl$_3$ at a concentration of 1 mg/mL (exc. 800 nm). Insets (B1,B2) show the variation of the maximum of the emission wavelength and the maximum of the PL intensity as a function of solvent ratio. (C) PL decay curves of the different NPs. (D) Lifetimes and absolute QYs as a function of solvent ratio. The color legend is as follows: Ag$_2$S-0.00, cyan; Ag$_2$S-0.15, red; Ag$_2$S-0.30, green; Ag$_2$S-0.60, blue; Ag$_2$S-0.90, orange; and Ag$_2$S-1.00, black, with numeric values indicating the χ_{DDT}.

Subsequently, these NPs were covered with PEG-NH$_2$ (M_w= 5000 g/mol) via EDC/NHS coupling. To do that, 0.5 mg of EDC and 0.7 mg of sulfo-NHS were dissolved in 1 mL of PBS containing 1 mg of the previously prepared MUA functionalized Ag$_2$S/Ag and 1 mg of PEG-NH$_2$. The mixture was gently stirred for 2 h, and after that, the NPs were collected by centrifugation at 12,000 rpm for 2 h. This process was repeated three times and the resulting NPs were dispersed in 1 mL of PBS and stored at 4 °C.

3. RESULTS AND DISCUSSION

Figure 1 depicts the HAADF−STEM images of the Ag$_2$S NPs synthesized using different solvent ratios. As observed, all the NPs exhibit two well-differentiated regions, a white area with higher Z-contrast, corresponding to the electrodense parts of the NPs, probably due to the presence of metallic Ag into the NPs. In addition, the figure shows the existence of less electrodense areas that appear as gray regions, corresponding to Ag$_2$S.

The energy-dispersive spectrometry (EDS) elemental mappings showed in Figure 1 reveal the anisotropic spatial distribution of Ag (red) and S (green) within the NPs. These micrographs unveil the presence of Ag-enriched regions that overlap with those that exhibited higher Z-contrast (white regions in the HAADF−STEM micrographs). Interestingly, this silver core appears more eccentrically located when lower χ_{DDT} is used during the synthesis. The synthetic conditions induce variations in the structure and properties of the synthesized NPs. In fact, a decrease in overall NP size can be clearly correlated with an increase of χ_{DDT} during the reaction. Figure S2 shows the average size of each synthesis as well as the size of the electrodense region that corresponds to the silver core. This result can be explained in terms of the higher capacity of the DDT molecules to interact with the NPs

through the thiol group, which exhibits the highest binding energy toward noble metals (200 kJ/mol).[34] Therefore, a high χ_{DDT} (high amount of DDT) leads to an increased colloidal stability of small NPs formed during the course of the reaction and thus preventing the particles from aggregation, resulting in a smaller overall NP size.

The XRD patterns of these NPs reveal the presence of two crystalline phases, which could be attributed to monoclinic Ag$_2$S (JCPDS card no. 14-0072; lattice constants: a = 4.229 Å, b = 6.931 Å, and c = 7.862 Å) and cubic Ag (JCPDS card no. 04-0783; lattice constants: a = 4.0862 Å), as can be seen in Figure S3. A more detailed analysis of the XRD patterns can be found in the Supporting Information. With the aim of completing the structural and compositional characterization, X-ray photoelectron spectroscopy and XANE analysis have been carried out. The wide-scan survey spectra of the NPs show the presence of Ag 3d (364, 374 eV) and S 2p (161, 162.2 eV) doublets as well as C 1s (285 eV) and O 1s (532 eV). High-resolution scans of Ag 3d spectra are shown in Figure S4A. The deconvolution of the Ag 3d binding energy spectra is fitted with two silver doublets. The Ag$^+$ binding energy of the peaks centered at 372.2 eV (3d$_{3/2}$) and 366.6 eV (3d$_{5/2}$) could be attributed to Ag$_2$S, whereas those peaks at 373.6 eV (3d$_{3/2}$) and 367.5 eV (3d$_{5/2}$) could be related to Ag0, see Figure S4B. Complementary analyses by X-ray absorption near-edge structure (XANES) for the Ag K-edge spectra of the synthesized NPs have also been carried out. This technique permits determining the oxidation state of the Ag atoms that constitute the sample. The oxidation state of the samples was analyzed by a linear combination fitting procedure, as can be seen in Figure S6. The result of these analyses shows that in both cases, the NPs are constituted by a predominant phase of
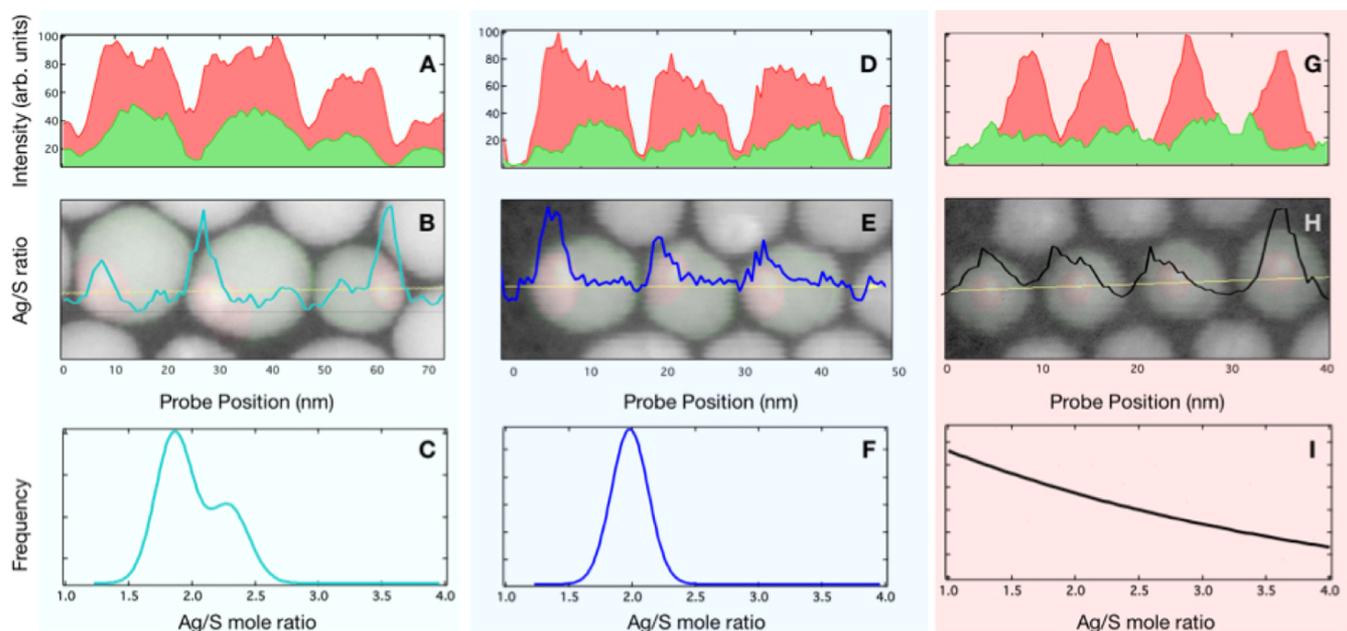
Figure 3. Net X-ray profile extracted from the yellow arrow marked in the STEM images (A,D,G). Merged STEM and NP model images represented as a function of Ag/S ratio vs the probe position (B,E,H). Frequency distribution of the Ag/S ratio in the NPs excluding the silver core (C,F,I). The NPs used for EDS mapping were derived using χ_{DDT} of 0.00 (A,C), 0.60 (D−F), and 1.00 (G−I) during the synthesis.

Ag_2S and a metallic Ag counterpart in a ratio 0.75:1. Furthermore, we have performed Fourier transform extended X-ray absorption fine structure of both types of NPs, as can be seen in Figure S7. As one can observe, both samples (Ag_2S-0.00 and Ag_2S-0.60) exhibit two main peaks, one located at 2 Å, which matches perfectly with the Ag−S distance in the Ag_2S phase, and a second peak located at 2.8 Å, which is characteristic of the Ag−Ag distance in the metallic Ag phase, and therefore, we can conclude that the synthesized Ag_2S NPs have a metallic Ag phase within the structure.

Figure 2 summarizes the impact of the synthetic conditions on the spectroscopic properties of the NPs (absorption, PL, lifetime, and QY). Figure 2A shows the normalized absorption spectra for all samples in the range between 300 and 900 nm. In all cases, a strong absorption in the visible region with a weak shoulder at 465 nm and a long tail until the NIR region can be observed. The shoulder at ∼465 nm may be attributed to the plasmonic contribution of the metallic Ag present in the NP.[35,36] It is important to note that this band only appears in those syntheses in which OLA is used. This indicates the role of the amino groups in the formation of metallic silver during the synthesis of NPs at high temperatures.[33] In fact, it is well known that during the synthesis of Ag_2S NPs through the thermal decomposition of a silver precursor, such as Ag-monothiobenzoate or Ag-diethyldithiocarbamate, metallic Ag nanocrystals are formed as the side products.[37,38] This is because the dissociation energy of the Ag−S bond (206.45 kJ/mol) is lower compared to that of the S−C bond (265.95 kJ/mol), and, under a heating up process, Ag ions are released in the absence of reactive sulfur.[39] The addition of alkylamines in the reaction may lower the dissociation energy of the S−C bonds of the silver precursor via nucleophilic addition of an amine to the carbonyl group, thereby potentially providing a higher amount of reactive sulfur in the reaction, resulting in an increase of the Ag_2S matrix size.[40] Such an effect can be observed in Figure S1; here, one can observe the reduction of

the size of the Ag_2S matrix when increasing the χ_{DDT}, while the size of the Ag core remains unchanged.

Figure 2B shows the emission band of the different samples as obtained under 800 nm optical excitation. The emission band is clearly affected by the synthesis conditions. First, we observe that the peak wavelength is red-shifted when increasing the χ_{DDT}. In fact, the NPs synthesized only in the presence of OLA exhibit its maximum emission at 1160 nm, while those synthesized using only DDT as a solvent showed its emission peak at 1220 nm. These variations indicate an increment in the band gap of the NPs when increasing the χ_{DDT}, which cannot be attributed to quantum confinement effects because the size of all these NPs are well above the Bohr radius of Ag_2S.[41,42] Another effect observed is a prominent variation of the luminescence emission intensity with χ_{DDT}, which could be related to different emission efficiencies. For a better understanding, the luminescence decay times of the NPs were measured, see Figure 2C. From these results, we can observe an enhancement of the NP lifetimes from 120 to 1200 ns when increasing the χ_{DDT} up to 0.60, see Figure 2D. Such an increment of the lifetimes is concomitant with the enhancement of the QY that increases from 0.2 to 2.3%. Surprisingly, a further increase of χ_{DDT} provoked a subsequent reduction of the lifetimes from 1200 to 180 ns as well as the QY values, from 2.4% down to 0.2%. For the lowest and the highest χ_{DDT} values, decreased PL lifetimes and QYs could be attributed to the increment of nonradiative pathways in the NPs. All these results allowed us to identify the optimal synthetic conditions for the production of highly efficient Ag_2S NPs.

In order to understand how synthetic conditions could affect the emission of the NPs, we have analyzed the composition of the generated NPs by EDS mapping profile, as can be seen in Figure 3. It is evidenced how the synthetic conditions affect tremendously the size, shape, position of the Ag-enriched core, and also the atomic ratio of Ag/S within the NPs. In fact, the analysis of the NET X-ray profile of those NPs synthesized with neat OLA (χ_{DDT} of 0.00, Figure 3A) allows to infer the
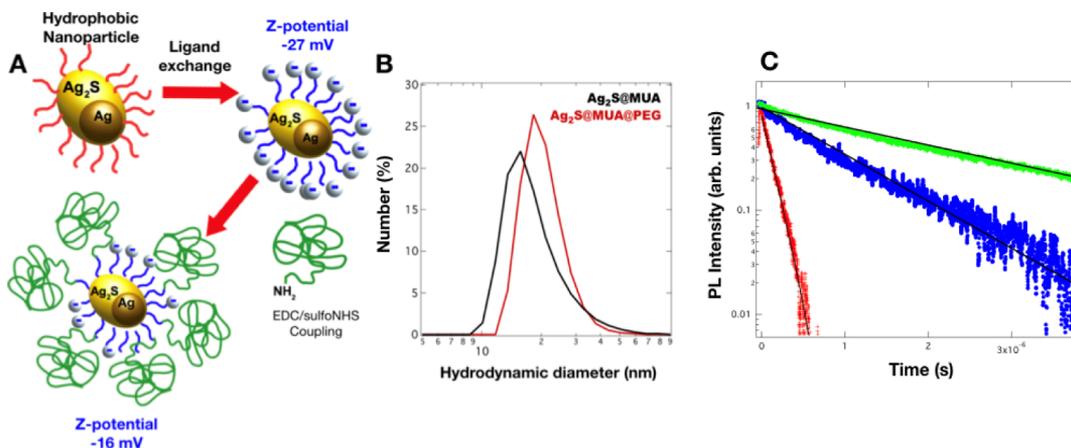
Figure 4. (A) Schematic representation for the surface modification of the NPs by ligand-exchange reaction with MUA and its subsequent PEGylation through the EDC/sulfo-NHS coupling reaction. Graphic (B) evolution of the NP hydrodynamic diameter during the surface functionalization process. (C) PL decay times of Ag_2S/Ag NPs in $CHCl_3$ (green), Ag_2S/Ag-PEG NPs in PBS at a concentration of 1 mg/mL (blue), and Ag_2S-PEG NPs synthesized by Zhang's method in PBS at a concentration of 1.5 mg/mL (red).
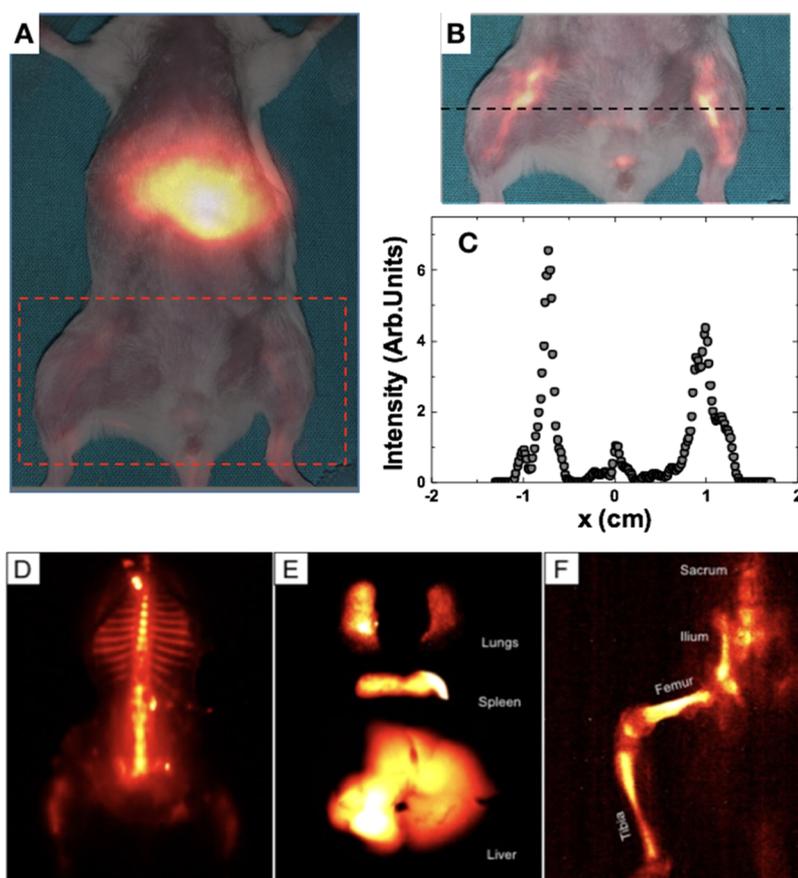

Figure 5. (A) In vivo imaging of an anesthetized mouse 5 min after intravenous injection of the thus optimized Ag_2S NPs. The animal was optically excited with an 800 nm laser diode with a power density of 45 mW/cm², and luminescence (1000−1400 nm) was recorded with an infrared camera. (B) Magnification of the lower extremities where the femoral vessels can be observed. (C) Cross-sectional intensity profile measured along the black dashed line in (B). (D) Ex vivo NIR-II image of the skeleton and (E) lungs, spleen, and liver of the dissected mouse and (F) detailed image of femur, tibia, ilium, and sacrum of mice.

Ag/S atomic ratio profile of such NPs as can be seen in Figure 3B that is characterized by the presence of peaks that match with the position of the silver-enriched region, while the rest of the regions present Ag/S atomic ratios around 2. When we represent the frequency distribution of the Ag/S ratio obtained in these NPs, we can observe the presence of two Gaussian populations, one centered at 1.8 and the other at 2.2, which differs from a theoretical ratio of 2, which should correspond to a perfect Ag_2S matrix (Figure 3C). Such a result would indicate the presence of compositional inhomogeneities in the Ag_2S matrix that could render in structural defects. This fact would explain the low QY observed in this sample.[43]

Interestingly, those NPs synthesized using a χ_{DDT} of 0.60 depict the NET X-ray profile different from the previous NPs, see Figure 3D. That informs us about Ag/S ratios close to 2, for those areas distinct to the silver-enriched regions, as can be seen in Figure 3E. When we represent the frequency distribution of the Ag/S ratio, we obtain a mean value centered at 1.9, which is closer to the hypothetical ratio of 2 of the Ag_2S matrix and would indicate the reduction of possible defects as shown in Figure 3F. This would be the reason why these NPs exhibit an increment of the static emission as well as the PL lifetime and QY. Finally, in the case of those NPs synthesized in the presence of neat DDT (χ_{DDT} of 1.00), the NET X-ray profile shows the presence of a high concentration of silver, located preferentially in the core of the NPs, Figure 3G. Such a profile creates a rapid increment of the Ag/S atomic ratio from a S-enriched surface to a Ag-enriched core, resulting in a very small region where the matrix composition could be Ag_2S, decreasing the NIR fluorescence of these NPs, as shown in Figure 3H. On the contrary, the frequency distribution of the Ag/S ratio does not permit us to observe any maximum close to 2, which would indicate the presence of a thin Ag_2S region surrounded by structural defects, which would render Ag_2S NPs with poor luminescent properties as observed in Figure 3I.

The optimized (from synthesis with χ_{DDT} of 0.60 with largest QY and luminescence lifetime) Ag_2S NPs were tested as NIR-II in vivo imaging contrast agents. To do that, a ligand-exchange reaction is carried out to substitute the hydrophobic capping agents by hydrophilic, thiol-bearing molecules for their stabilization in aqueous media. Figure 4A shows the ligand-exchange process. In the first step, carboxylic acid terminated MUA ligands are introduced on the surface of the NPs, thereby acquiring negative charges which are confirmed by the zeta potential measurements giving a value of $\sim$−27 mV. The hydrodynamic diameter of the MUA-functionalized NPs is 14 ± 7 nm in PBS. After that, carboxylic groups were used as anchoring points, allowing for the linkage of PEG-NH$_2$ molecules (5 kDa) through the amino-terminated group, performing a coupling reaction mediated by EDC and sulfo-NHS. The products of this reaction are PEG-modified NPs with a hydrodynamic diameter of 20 ± 9 nm and a zeta potential of −16 mV, which is still negative because of the presence of the remaining carboxylate groups on the surface of the NPs that did not react with PEG, as can be seen in Figure 4. After the ligand-exchange reaction, the luminescence lifetime decreased. As evident in Figure 4C, when these NPs were coated with PEG and transfer to PBS, the lifetime suffered a reduction from 1200 ns down to 379 ns. The observed reduction of the lifetime can be associated with the environment-assisted multiphoton relaxation processes, when the NPs are dispersed in water, as it was previously observed.[24] For the sake of comparison, we also measured the luminescence decay time of commercially available Ag_2S-PEG NPs in PBS (see Figure 4C). Note that our "optimized" Ag_2S NPs showed a significantly increased luminescence decay time, revealing the effective reduction of nonradiative decays because of the improved Ag and S ratio in the final matrix.

In order to demonstrate the potential of the "optimized" Ag_2S NPs for in vivo imaging, 150 μL of a solution with a NP concentration of 1 mg/mL was injected in 1 month-old CD1 female mice via retro-orbital injection. The anesthetized mouse was illuminated with a low-power 800 nm laser diode providing an on-target laser power density as low as 45

mW/cm^2. The luminescence generated by the Ag_2S NPs was registered by an InGaAs infrared camera. In order to avoid any contribution of laser-reflected light to the fluorescence image, a 1000 nm long-pass filter was used. In Figure 5A, an optical plus infrared fluorescence-merged image of the mouse, as obtained 5 min after the injection of the NPs, is shown. A clear luminescence signal is detected at the abdominal area of the mouse, which is attributed to a fast accumulation of NPs in the liver. Although the highest intensity is detected from the liver, a detailed inspection of the subabdominal region also reveals clear fluorescence contrast. The zoom included in Figure 5B reveals the presence of NPs in the bloodstream. In particular, vessels of the lower limbs are evident in the amplified fluorescence image. Indeed, it is clear that, even by using this low excitation power density and low magnification optics, the optimized Ag_2S NPs are bright enough to provide an image of the vessel anatomy with a submillimeter spatial resolution (see intensity profile in Figure 5C). In order to elucidate the biodistribution of the injected NPs, the animal was sacrificed 1 h after injection, and the presence of Ag_2S in the different organs was elucidated from their fluorescence images. Figure 5D shows the fluorescence image corresponding to the skeleton, indicating the partial accumulation of Ag_2S NPs within the bones. Figure 5E includes the infrared fluorescence images corresponding to the liver, spleen, and lungs. Only these organs provided any relevant infrared fluorescence. This fact indicates that 1 h postinjection, the Ag_2S NPs were accumulated at the bones, lungs, liver, and spleen. Similar biodistribution patterns were already reported by other authors.[44,45] Finally, Figure 5F shows an amplified fluorescence image of the bone structure of a limb. Note how the accumulation of Ag_2S NPs at the bones opens the way of obtaining high-resolution images of the skeleton by infrared fluorescence imaging. At this point, we would like to stress that the accumulation of Ag_2S NPs at bone structures could not only be used for advanced in vivo imaging of the bone structure but it can also be used for therapeutic effects. Note that Ag_2S NPs are also known to be excellent luminescent nanothermometers. This means that they could be potentially used to measure the intrabone temperature. This, in turns, becomes essential to achieve full control over photothermal therapies of bones, which have been recently demonstrated to be of high efficacy to promote bone regeneration.[46−48]

4. CONCLUSIONS

The present work demonstrates the crucial role of the synthetic conditions on the PL properties of Ag_2S NPs. More in detail, the effect of the solvent ratio of DDT and OLA during the NP generation via thermal degradation using Ag(DDTC) was evaluated. In total, six different solvent ratios were tested (χ_{DDT} of 0.00, 0.15, 0.30, 0.60, 0.90, and 1.00). From a structural point of view, a clear decrease in NP size with an increase of DDT was observed, assumingly correlated with a more pronounced stabilization of small NPs by the thiol-bearing solvent DDT. Regarding the photoluminescent properties, a maximum of luminescence lifetimes and QY was observed for NPs generated with a χ_{DDT} of 0.60. The measured luminescence lifetimes reached values of 1200 ns in comparison to lifetimes of 120 and 180 ns for the NPs synthesized using χ_{DDT} of 0.00 and 1.00, respectively. For the QY, a 10-fold higher value of 2.3% was determined for the NPs synthesized with a χ_{DDT} of 0.60 compared to the NPs derived from neat solvents. As studied by the EDS mapping of the

generated NPs using χ_{DDT} of 0.00, 0.60, and 1.00, we were able to clearly correlate the improved photoluminescent properties to a more precise ratio of Ag and S in the final NP matrix. In addition, the surface modification of the Ag_2S NPs allows for a transfer into aqueous solution. In this media, our fabricated Ag_2S NPs conserve the superb optical properties, exhibiting higher luminescence lifetimes and QY compared to commercially available PEGylated Ag_2S in aqueous buffer. This permits their usage as contrast imaging agents, where the NPs present an excellent biodistribution.

■ ASSOCIATED CONTENT

Ⓢ Supporting Information

The Supporting Information is available free of charge at https://pubs.acs.org/doi/10.1021/acsami.9b22827.

Chemical conditions; XRD characterization; XPS, XANES, and Fourier transform EXAFS; PLQY measurements; and dose-dependent experiment and performance (PDF)

■ AUTHOR INFORMATION

Corresponding Authors

Rafael Contreras-Cáceres − *Departamento de Química en Ciencias Farmacéuticas, Universidad Complutense de Madrid, Madrid 28040, Spain;* ◎ orcid.org/0000-0001-6313-2340; Email: rcontreras@uma.es

Daniel Jaque − *Nanobiology Group, Instituto Ramón y Cajal de Investigación Sanitaria, IRYCIS, Madrid 28034, Spain; Fluorescence Imaging Group, Facultad de Ciencias, Universidad Autónoma de Madrid, Madrid 28049, Spain;* ◎ orcid.org/0000-0002-3225-0667; Email: daniel.jaque@uam.es

Jorge Rubio-Retama − *Nanobiology Group, Instituto Ramón y Cajal de Investigación Sanitaria, IRYCIS, Madrid 28034, Spain; Departamento de Química en Ciencias Farmacéuticas, Universidad Complutense de Madrid, Madrid 28040, Spain;* ◎ orcid.org/0000-0002-1785-5844; Email: bjrubio@ucm.es

Authors

Alicia Ortega-Rodríguez − *Departamento de Química en Ciencias Farmacéuticas, Universidad Complutense de Madrid, Madrid 28040, Spain; Departamento Química Orgánica, Facultad de Ciencias, Universidad de Málaga, Málaga 29071, Spain*

Yingli Shen − *Nanobiology Group, Instituto Ramón y Cajal de Investigación Sanitaria, IRYCIS, Madrid 28034, Spain; Fluorescence Imaging Group, Facultad de Ciencias, Universidad Autónoma de Madrid, Madrid 28049, Spain*

Irene Zabala Gutierrez − *Departamento de Química en Ciencias Farmacéuticas, Universidad Complutense de Madrid, Madrid 28040, Spain*

Harrison D. A. Santos − *Nanobiology Group, Instituto Ramón y Cajal de Investigación Sanitaria, IRYCIS, Madrid 28034, Spain; Fluorescence Imaging Group, Facultad de Ciencias, Universidad Autónoma de Madrid, Madrid 28049, Spain*

Vivian Torres Vera − *Departamento de Química en Ciencias Farmacéuticas, Universidad Complutense de Madrid, Madrid 28040, Spain*

Erving Ximendes − *Nanobiology Group, Instituto Ramón y Cajal de Investigación Sanitaria, IRYCIS, Madrid 28034, Spain; Fluorescence Imaging Group, Facultad de Ciencias, Universidad Autónoma de Madrid, Madrid 28049, Spain*

Gonzalo Villaverde − *Departamento de Química en Ciencias Farmacéuticas, Universidad Complutense de Madrid, Madrid 28040, Spain*

José Lifante − *Nanobiology Group, Instituto Ramón y Cajal de Investigación Sanitaria, IRYCIS, Madrid 28034, Spain; Fluorescence Imaging Group, Facultad de Ciencias, Universidad Autónoma de Madrid, Madrid 28049, Spain*

Christoph Gerke − *Departamento de Química en Ciencias Farmacéuticas, Universidad Complutense de Madrid, Madrid 28040, Spain*

Nuria Fernández − *Nanobiology Group, Instituto Ramón y Cajal de Investigación Sanitaria, IRYCIS, Madrid 28034, Spain; Fluorescence Imaging Group, Facultad de Ciencias, Universidad Autónoma de Madrid, Madrid 28049, Spain*

Oscar G. Calderón − *Departamento de Óptica, Universidad Complutense de Madrid, Madrid 28037, Spain*

Sonia Melle − *Departamento de Óptica, Universidad Complutense de Madrid, Madrid 28037, Spain;* ◎ orcid.org/0000-0002-9802-6908

José Marques-Hueso − *Institute of Sensors, Signals and Systems (ISSS), School of Engineering & Physical Sciences (EPS), Heriot-Watt University, Edinburgh EH15 2BR, United Kingdom*

Diego Mendez-Gonzalez − *Departamento de Química en Ciencias Farmacéuticas, Universidad Complutense de Madrid, Madrid 28040, Spain*

Marco Laurenti − *Nanobiology Group, Instituto Ramón y Cajal de Investigación Sanitaria, IRYCIS, Madrid 28034, Spain; Departamento de Química en Ciencias Farmacéuticas, Universidad Complutense de Madrid, Madrid 28040, Spain;* ◎ orcid.org/0000-0002-0273-7423

Callum M. S. Jones − *Institute of Sensors, Signals and Systems (ISSS), School of Engineering & Physical Sciences (EPS), Heriot-Watt University, Edinburgh EH15 2BR, United Kingdom*

Juan Manuel López-Romero − *Departamento Química Orgánica, Facultad de Ciencias, Universidad de Málaga, Málaga 29071, Spain*

Complete contact information is available at:
https://pubs.acs.org/10.1021/acsami.9b22827

Notes

The authors declare no competing financial interest.

■ ACKNOWLEDGMENTS

■ REFERENCES

(1) Qin, M.-Y.; Yang, X.-Q.; Wang, K.; Zhang, X.-S.; Song, J.-T.; Yao, M.-H.; Yan, D.-M.; Liu, B.; Zhao, Y.-D. In vivo cancer targeting and fluorescence-CT dual-mode imaging with nanoprobes based on silver sulfide quantum dots and iodinated oil. *Nanoscale* **2015**, *7*, 19484−19492.

(2) Key, J.; Leary, J. Nanoparticles for multimodal in vivo imaging in nanomedicine. *Int. J. Nanomed.* **2014**, *9*, 711−726.

(3) Chen, Z.-Y.; Wang, Y.-X.; Yang, F.; Lin, Y.; Zhou, Q.-L.; Liao, Y.-Y.; Liao, Y. Y. Advance of molecular imaging technology and targeted imaging agent in imaging and therapy. *BioMed Res. Int.* **2014**, *2014*, 1−22.

(4) Wang, X.; Pang, Y.; Ku, G.; Xie, X.; Stoica, G.; Wang, L. V. Noninvasive laser-induced photoacoustic tomography for structural and functional in vivo imaging of the brain. *Nat. Biotechnol.* **2003**, *21*, 803−806.

(5) Hong, G.; Antaris, A. L.; Dai, H. Near-infrared fluorophores for biomedical imaging. *Nat. Biomed. Eng.* **2017**, *1*, 1−22.

(6) Frangioni, J. In vivo near-infrared fluorescence imaging. *Curr. Opin. Chem. Biol.* **2003**, *7*, 626−634.

(7) Zhao, J.; Zhong, D.; Zhou, S. NIR-I-to-NIR-II fluorescent nanomaterials for biomedical imaging and cancer therapy. *J. Mater. Chem. B* **2018**, *6*, 349−365.

(8) Hu, F.; Li, C.; Zhang, Y.; Wang, M.; Wu, D.; Wang, Q. Real-time in vivo visualization of tumor therapy by a near-infrared-II Ag2S quantum dot-based theranostic nanoplatform. *Nano Res.* **2015**, *8*, 1637−1647.

(9) Ortgies, D. H.; García-Villalón, Á. L.; Granado, M.; Amor, S.; Rodríguez, E. M.; Santos, H. D. A.; Yao, J.; Rubio-Retama, J.; Jaque, D. Infrared fluorescence imaging of infarcted hearts with Ag2S nanodots. *Nano Res.* **2019**, *12*, 749−757.

(10) Diao, S.; Blackburn, J. L.; Hong, G.; Antaris, A. L.; Chang, J.; Wu, J. Z.; Zhang, B.; Cheng, K.; Kuo, C. J.; Dai, H. Fluorescence Imaging In Vivo at Wavelengths beyond 1500 nm. *Angew. Chem., Int. Ed. Engl.* **2015**, *54*, 14758−14762.

(11) Antaris, A. L.; Chen, H.; Cheng, K.; Sun, Y.; Hong, G.; Qu, C.; Diao, S.; Deng, Z.; Hu, X.; Zhang, B.; Zhang, X.; Yaghi, O. K.; Alamparambil, Z. R.; Hong, X.; Cheng, Z.; Dai, H. A small-molecule dye for NIR-II imaging. *Nat. Mater.* **2016**, *15*, 235−242.

(12) Welsher, K.; Liu, Z.; Sherlock, S. P.; Robinson, J. T.; Chen, Z.; Daranciang, D.; Dai, H. A route to brightly fluorescent carbon nanotubes for near-infrared imaging in mice. *Nat. Nanotechnol.* **2009**, *4*, 773−780.

(13) Fernée, M. J.; Thomsen, E.; Jensen, P.; Rubinsztein-Dunlop, H. Highly efficient luminescence from a hybrid state found in strongly quantum confined PbS nanocrystals. *Nanotechnology* **2006**, *17*, 956−962.

(14) Greben, M.; Fucikova, A.; Valenta, J. Photoluminescence quantum yield of PbS nanocrystals in colloidal suspensions. *J. Appl. Phys.* **2015**, *117*, 144306.

(15) Rzigalinski, B. A.; Strobl, J. S. Cadmium-containing nanoparticles: perspectives on pharmacology and toxicology of quantum dots. *Toxicol. Appl. Pharmacol.* **2009**, *238*, 280−288.

(16) Liu, W.; Zhang, S.; Wang, L.; Qu, C.; Zhang, C.; Hong, L.; Yuan, L.; Huang, Z.; Wang, Z.; Liu, S.; Jiang, G. CdSe quantum dot (QD)-induced morphological and functional impairments to liver in mice. *PLoS One* **2011**, *6*, No. e24406.

(17) Hong, G.; Robinson, J. T.; Zhang, Y.; Diao, S.; Antaris, A. L.; Wang, Q.; Dai, H. In vivo fluorescence imaging with Ag2S quantum dots in the second near-infrared region. *Angew. Chem., Int. Ed. Engl.* **2012**, *51*, 9818−9821.

(18) Dong, B.; Li, C.; Chen, G.; Zhang, Y.; Zhang, Y.; Deng, M.; Wang, Q. Facile Synthesis of Highly Photoluminescent Ag2Se Quantum Dots as a New Fluorescent Probe in the Second Near-Infrared Window for in Vivo Imaging. *Chem. Mater.* **2013**, *25*, 2503−2509.

(19) Liu, Y.-W.; Ko, D.-K.; Oh, S. J.; Gordon, T. R.; Doan-Nguyen, V.; Paik, T.; Kang, Y.; Ye, X.; Jin, L.; Kagan, C. R.; Murray, C. B. Near-Infrared Absorption of Monodisperse Silver Telluride (Ag2Te) Nanocrystals and Photoconductive Response of Their Self-Assembled Superlattices. *Chem. Mater.* **2011**, *23*, 4657−4659.

(20) Shen, Y.; Lifante, J.; Ximendes, E.; Santos, H. D. A.; Ruiz, D.; Juárez, B. H.; Zabala Gutiérrez, I.; Torres Vera, V.; Rubio Retama, J.; Martín Rodríguez, E.; Ortgies, D. H.; Jaque, D.; Benayas, A.; Del Rosal, B. Perspectives for Ag2S NIR-II nanoparticles in biomedicine: from imaging to multifunctionality. *Nanoscale* **2019**, *11*, 19251−19264.

(21) Lu, F.; Gong, Y.; Ju, W.; Cheng, F.; Zhang, K.; Wang, Q.; Wang, W.; Zhong, J.; Fan, Q.; Huang, W. Facile one-pot synthesis of monodispersed NIR-II emissive silver sulfide quantum dots. *Inorg. Chem. Commun.* **2019**, *106*, 233−239.

(22) Ruiz, D.; Mizrahi, M.; Santos, H. D. A.; Jaque, D.; Jones, C. M. S.; Marqués-Hueso, J.; Jacinto, C.; Requejo, F. G.; Torres-Pardo, A.; González-Calbet, J. M.; Juárez, B. H. Synthesis and characterization of Ag2S and Ag2S/Ag2(S,Se) NIR nanocrystals. *Nanoscale* **2019**, *11*, 9194−9200.

(23) Jiang, P.; Tian, Z.-Q.; Zhu, C.-N.; Zhang, Z.-L.; Pang, D.-W. Emission-Tunable Near-Infrared Ag2S Quantum Dots. *Chem. Mater.* **2011**, *24*, 3−5.

(24) Santos, H. D. A.; Ruiz, D.; Lifante, G.; Jacinto, C.; Juarez, B. H.; Jaque, D. Time resolved spectroscopy of infrared emitting Ag2S nanocrystals for subcutaneous thermometry. *Nanoscale* **2017**, *9*, 2505−2513.

(25) Zhang, Y.; Liu, Y.; Li, C.; Chen, X.; Wang, Q. Controlled Synthesis of Ag2S Quantum Dots and Experimental Determination of the Exciton Bohr Radius. *J. Phys. Chem. C* **2014**, *118*, 4918−4923.

(26) Giansante, C.; Infante, I. Surface Traps in Colloidal Quantum Dots: A Combined Experimental and Theoretical Perspective. *J. Phys. Chem. Lett.* **2017**, *8*, 5209−5215.

(27) Boles, M. A.; Ling, D.; Hyeon, T.; Talapin, D. V. Erratum: The surface science of nanocrystals. *Nat. Mater.* **2016**, *15*, 364.

(28) Doh, H.; Hwang, S.; Kim, S. Size-Tunable Synthesis of Nearly Monodisperse Ag2S Nanoparticles and Size-Dependent Fate of the Crystal Structures upon Cation Exchange to AgInS2 Nanoparticles. *Chem. Mater.* **2016**, *28*, 8123−8127.

(29) Ruiz, D.; del Rosal, B.; Acebrón, M.; Palencia, C.; Sun, C.; Cabanillas-González, J.; López-Haro, M.; Hungría, A. B.; Jaque, D.; Juarez, B. H. Ag/Ag2S Nanocrystals for High Sensitivity Near-Infrared Luminescence Nanothermometry. *Adv. Funct. Mater.* **2017**, *27*, 1604629.

(30) Sadovnikov, S. I.; Kuznetsova, Y. V.; Rempel, A. A. Ag2S silver sulfide nanoparticles and colloidal solutions: Synthesis and properties. *Nano-Struct. Nano-Objects* **2016**, *7*, 81−91.

(31) Zhang, Y.; Hong, G.; Zhang, Y.; Chen, G.; Li, F.; Dai, H.; Wang, Q. Ag2S Quantum Dot: A Bright and Biocompatible Fluorescent Nanoprobe in the Second Near-Infrared Window. *ACS Nano* **2012**, *6*, 3695−3702.

(32) He, H.; Lin, Y.; Tian, Z.-Q.; Zhu, D.-L.; Zhang, Z.-L.; Pang, D.-W. Ultrasmall Pb:Ag2 S Quantum Dots with Uniform Particle Size and Bright Tunable Fluorescence in the NIR-II Window. *Small* **2018**, *14*, 1703296.

(33) Liu, W.; Zhang, J.; Peng, Z.; Yang, X.; Li, L.; Chen, Q.; Liu, J.; Wang, K. Controlled formation of Ag2S/Ag Janus nanoparticles using alkylamine as reductant surfactants. *Colloids Surf., A* **2018**, *544*, 111−117.

(34) Love, J. C.; Estroff, L. A.; Kriebel, J. K.; Nuzzo, R. G.; Whitesides, G. M. Self-Assembled Monolayers of Thiolates on Metals as a Form of Nanotechnology. *Chem. Rev.* **2005**, *105*, 1103−1169.

(35) Mogensen, K. B.; Kneipp, K. Size-Dependent Shifts of Plasmon Resonance in Silver Nanoparticle Films Using Controlled Dissolution: Monitoring the Onset of Surface Screening Effects. *J. Phys. Chem. C* **2014**, *118*, 28075−28083.

(36) Serrano-Montes, A. B.; Jimenez de Aberasturi, D.; Langer, J.; Giner-Casares, J. J.; Scarabelli, L.; Herrero, A.; Liz-Marzán, L. M. A General Method for Solvent Exchange of Plasmonic Nanoparticles and Self-Assembly into SERS-Active Monolayers. *Langmuir* **2015**, *31*, 9205−9213.

(37) Tang, Q.; Yoon, S. M.; Yang, H. J.; Lee, Y.; Song, H. J.; Byon, H. R.; Choi, H. C. Selective degradation of Chemical Bonds: from Single-Source Molecular Precursor to Metallic Ag and Semiconducting Ag2S Nanocrystals via Instant Thermal Activation. *Langmuir* **2006**, *22*, 2802−2805.

(38) Du, Y.; Xu, B.; Fu, T.; Cai, M.; Li, F.; Zhang, Y.; Wang, Q. Near-Infrared Photoluminescent Ag2S Quantum Dots from a Single Source Precursor. *J. Appl. Chem. Sci.* **2010**, *132*, 1470−1471.

(39) Tang, Q.; Yoon, S. M.; Yang, H. J.; Lee, Y.; Song, H. J.; Byon, H. R.; Choi, H. C. Selective Degradation of Chemical Bonds: from Single-Source Molecular Precursors to Metallic Ag and Semiconducting Ag2S Nanocrystals via Instant Thermal Activation. *Langmuir* **2006**, *22*, 2802−2805.

(40) Lim, W. P.; Zhang, Z.; Low, H. Y.; Chin, W. S. Preparation of Ag(2)S nanocrystals of predictable shape and size. *Angew. Chem., Int. Ed.* **2004**, *43*, 5685−5689.

(41) Lin, S.; Feng, Y.; Wen, X.; Zhang, P.; Woo, S.; Shrestha, S.; Conibeer, G.; Huang, S. Theoretical and Experimental Investigation of the Electronic Structure and Quantum Confinement of Wet-Chemistry Synthesized Ag2S Nanocrystals. *J. Phys. Chem. C* **2014**, *119*, 867−872.

(42) Kashida, S. Electronic structure of Ag2S, band calculation and photoelectron spectroscopy. *Solid State Ionics* **2003**, *158*, 167−175.

(43) Wang, Z.; Gu, T.; Kadohira, T.; Tada, T.; Watanabe, S. Migration of Ag in low-temperature Ag2S from first principles. *J. Chem. Phys.* **2008**, *128*, 014704.

(44) Jiang, P.; Zhu, C.-N.; Zhang, Z.-L.; Tian, Z.-Q.; Pang, D.-W. Water-soluble Ag(2)S quantum dots for near-infrared fluorescence imaging in vivo. *Biomaterials* **2012**, *33*, 5130−5135.

(45) Zhang, Y.; Zhang, Y.; Hong, G.; He, W.; Zhou, K.; Yang, K.; Li, F.; Chen, G.; Liu, Z.; Dai, H.; Wang, Q. Biodistribution, pharmacokinetics and toxicology of Ag2S near-infrared quantum dots in mice. *Biomaterials* **2013**, *34*, 3639−3646.

(46) Yanagi, T.; Kajiya, H.; Kawaguchi, M.; Kido, H.; Fukushima, T. Photothermal stress triggered by near infrared-irradiated carbon nanotubes promotes bone deposition in rat calvarial defects. *J. Biomater. Appl.* **2015**, *29*, 1109−1118.

(47) Heo, D. N.; Ko, W.-K.; Bae, M. S.; Lee, J. B.; Lee, D.-W.; Byun, W.; Lee, C. H.; Kim, E.-C.; Jung, B.-Y.; Kwon, I. K. Enhanced bone regeneration with a gold nanoparticle−hydrogel complex. *J. Mater. Chem. B* **2014**, *2*, 1584−1593.

(48) Wang, Y.; Hu, X.; Zhang, L.; Zhu, C.; Wang, J.; Li, Y.; Wang, Y.; Wang, C.; Zhang, Y.; Yuan, Q. Bioinspired extracellular vesicles embedded with black phosphorus for molecular recognition-guided biomineralization. *Nat. Commun.* **2019**, *10*, 2829−2839.